Finite element model for micro-stamping titanium bipolar plate

KHADEMI Maziar[1,a], ZHANG Peng Neo[1,b] *, PEREIRA Michael[2,c],
SREENIVAS Achuth[1,d] and WEISS Matthias[1,e]

[1]Deakin University, Institute for Frontier Materials, Waurn Ponds, Pigdons Rd., Geelong,VIC. 3216, Australia

[2]Deakin University, School of Engineering, Waurn Ponds, Pigdons Rd., Geelong,VIC. 3216, Australia

[a]maziar.khademi@gmail.com; [b]zhangp@deakin.edu.au, [c]michael.pereira@deakin.edu.au, [d]achut@deakin.edu.au, [e]matthias.weiss@deakin.edu.au

Keywords: Bipolar Plates, Micro-Stamping, Thin Foil, Finite Element Method

Abstract. Bipolar plates are the essential components of a Proton Exchange Membrane Fuel Cell. Lightweight bipolar plates can be micro-stamped from an ultrathin metallic foil. A major concern is the manufacturability of the foil in the micro-stamping process. The typical stamped micro-channels have end cavities or corners where the deformation mode can be different from the two-dimensional plane strain conditions that occur at the straight sections of the micro-channels. The thin foil has a large ratio of length (or width) to thickness, and shell elements were often used for three-dimensional models. Currently, it is unknown if the shell elements available in commercial software packages are able to predict the ultrathin material behaviour correctly. In addition, the deformation behaviour and forming limits of titanium foil in the micro-stamping process are not well understood. The current study uses a micro-stamping tool to produce straight micro-channels from commercially pure titanium foil. The experimental data are used to validate a two-dimensional and a three-dimensional finite element model of the process. It is shown that there are deviations between the experimental and the numerical thinning results. Material thinning is different between the straight and the cavity end sections suggesting that three-dimensional process models are required to accurately analyze forming.

Introduction

Fuel cells are capable of producing clean energy and reducing greenhouse gas emissions and are considered a suitable alternative to internal combustion engines [1]. The bipolar plate is an essential component of the Proton Exchange Membrane Fuel Cells (PEMFC) to distribute gas (hydrogen, air) uniformly through micro-channels and to conduct current [2].

Bipolar plates can be made of various materials, and metal bipolar plates have been considered to reduce weight and enable high-volume manufacture at low cost [3]. Aluminium alloys [4], titanium [5], and stainless steel [6] have been applied for metal bipolar plates and formed with stamping [7], rubber pad forming [8], and hydroforming [9]. Liu and Hua [10] applied rubber pad forming to manufacture multi-row micro-channels from SS304. They investigated process control parameters (rubber hardness, internal and outer radii, draft angle) by two-dimensional (2D) finite element (FE) simulation. Kolahdooz et al. [11] studied the rubber pad forming of SS316L bipolar plates with 0.1 mm thickness and considered three-dimensional (3D) shell elements in their simulation. Osia et al. [12] used a 3D FE model to investigate two convex and concave hydroforming methods to form SS304 bipolar plates. Bong et al. [13] implemented a multi-stage micro stamping process and according to the major deformation mode of plane strain employed 2D plane strain elements in the numerical analysis. In contrast, Karacan et al. [14] applied 3D shell elements to study the forming of different channel depths in micro stamping. They found that the dominant stress state in micro-stamping was a combination of biaxial and plane strain. Modanloo

et al. [15] studied the micro stamping of titanium bipolar plates with parallel flow channels and predicted fracture using different ductile fracture criteria in combination with a 3D FE model.

Typical stamped micro-channels have end cavities or corners where the deformation mode can be distinctly different from the two-dimensional (2D) plane strain that occurs in the straight U-section profile of the micro-channels[16]. This requires 3D models to represent the different deformation conditions. The thin foil has a large ratio of length (or width) to thickness, and shell elements are often used for 3D models. However, limited research has been done to study the effect of the element type on the thinning or strain predictions in micro stamping. Currently, it is unknown if shell elements available in commercial software packages can predict the ultrathin material behaviour correctly. The situation becomes more complicated when analysing the forming of titanium foil. The current study uses a micro-stamping tool to produce straight micro-channels from commercially pure titanium foil. The experimental data are then used to validate a 3D FE model of the process. The findings of this study will help guide future FE analysis and will give insights into the micro-stamping of titanium foil.

Material Properties
A commercially-pure titanium (CP-Ti) foil with a thickness of 0.1 mm was used. To determine the tensile properties of the titanium sheet, samples were prepared at 0° to the rolling direction and tensile tests were performed based on the ASTM standard (E8M-04) [17]. "Orange peel" was obtained on the dogbone sample surfaces after the tensile tests, which indicates that the limited number of grains within the thickness may lead to local deformation before fracture [18]. The true stress-strain curve was determined, and the Swift law (Eq. 1) fitted to the plastic part of the curve, as shown in Fig. 1. In future work, a biaxial stretching experiment will be conducted for fitting the Swift law at a larger plastic range.
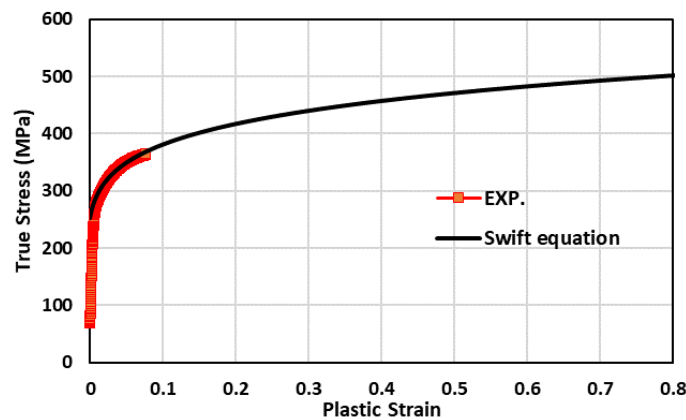

Fig. 1. True stress-strain curve and calibrated swift law results of Titanium foil

$$\sigma = K(\varepsilon + \varepsilon_0)^n \tag{1}$$

where σ and ε are the true stress and plastic strain obtained from the uniaxial tensile test. k, n and ε_0 are the constants of a particular material. The mechanical properties are listed in Table 1.

Table 1. Mechanical properties of the titanium sheet.

	E (GPa)	υ	K (MPa)	n	ε_0
titanium	120[15]	0.361[15]	517.2	0.135	0.005

Experimental Tests
The micro stamping tool was installed in an Instron 500 kN universal testing machine. A CP-Ti strip with dimensions of 195 mm × 97.5 mm was guillotined from the coil and the rolling direction

was aligned with the transverse direction of the channel. Fig. 2 presents the experimental setup [16]. Fig. 3 illustrates the dimensions of the designed micro-channels.
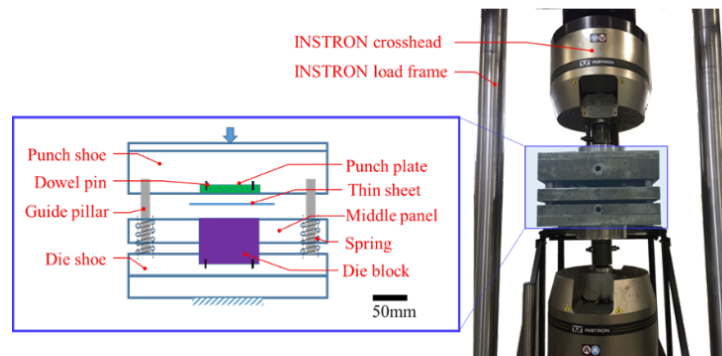

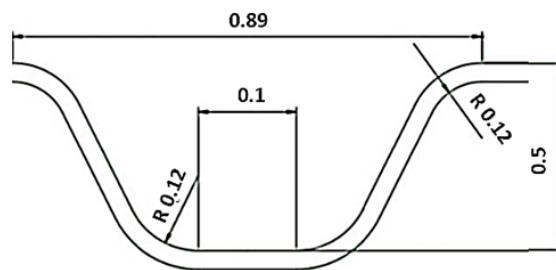*Fig. 2. The experimental equipment for the micro stamping trials [16].*

Fig. 3. Schematic of cross-section shape of one micro-channel, units in mm.

The top crosshead travelled at a load-controlled speed of 35 kN/min. The tests were stopped at a force of 90kN when cracks were found on all seven micro-channels and then repeated with more tests that stopped at sequentially reduced loads. After each test, the formed sheet was taken out for crack examination using the white-light method [16]. This identified a pinhole at a load of 78 kN (Fig. 4). The punch (male tooling) displacement at fracture initiation of the sheet was determined using an Alicona profilometer and determined to be approximately 0.32 mm when the pinhole initiated.

(a)   (b)
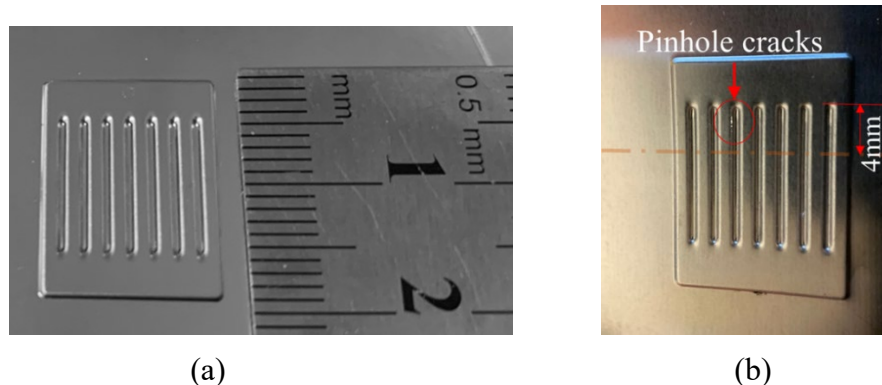
Fig. 4. CP-Ti bipolar micro channel plate produced by micro-stamping. (a) Formed without cracks and (b) with pinhole cracks, the location of cross-section for microscope observation is 4mm from the end cavities.

For evaluating the thinning, a segment of the sample was cut from the formed sheet at the cutting location marked in Figure 4-b. Then the sample was mounted in resin, ground and polished to a flat surface. An Olympus DP71 microscope with a digital camera system was used to capture images at 5× magnification (Fig. 5). The thickness was measured based on the captured image. A

line perpendicular to both sides of the surfaces was constructed at each measurement location, and the line length was measured [19] with Digimizer Image Analysis software [20]. This measurement approach can achieve subpixel (~0.001mm) accuracy. The thinning values are measured from two different channels (No. 2 & 3 in Fig. 5) and the averaged value is presented in this paper
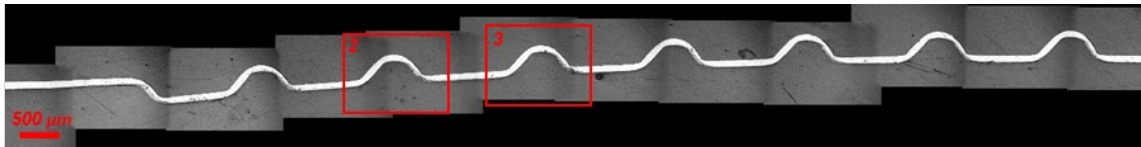

Fig. 5. Microscope image of a cross-section of the micro-stamped channel titanium

In this research, the thinning is used as the target parameter. Therefore, the thinning is defined as:

$$\%Thinning = \frac{t_0 - t_f}{t_0} \tag{2}$$

where t_0 is the initial blank thickness, and t_f is the thickness of the final formed part.

The forming die (female tooling) surfaces were also scanned, and Fig. 6-a and b show the 3D image of the surface scan obtained with the Alicona for one single corrugation. The cross-section tool profiles in the transverse and the longitudinal direction were determined by performing a section cut on the scanned 3D surface, as illustrated in Fig. 6-c and d. In this study the point cloud of the tool surface scan of the top and bottom die was used to generate the tool surfaces in the FE model. For this, the tool radii were approximated with smooth arcs, and the radii of the punch and die represent the best fit from a group of 10 points distributed at the corner. The tool dimensions and geometric features of the experimental set up are shown in Fig. 6-d.
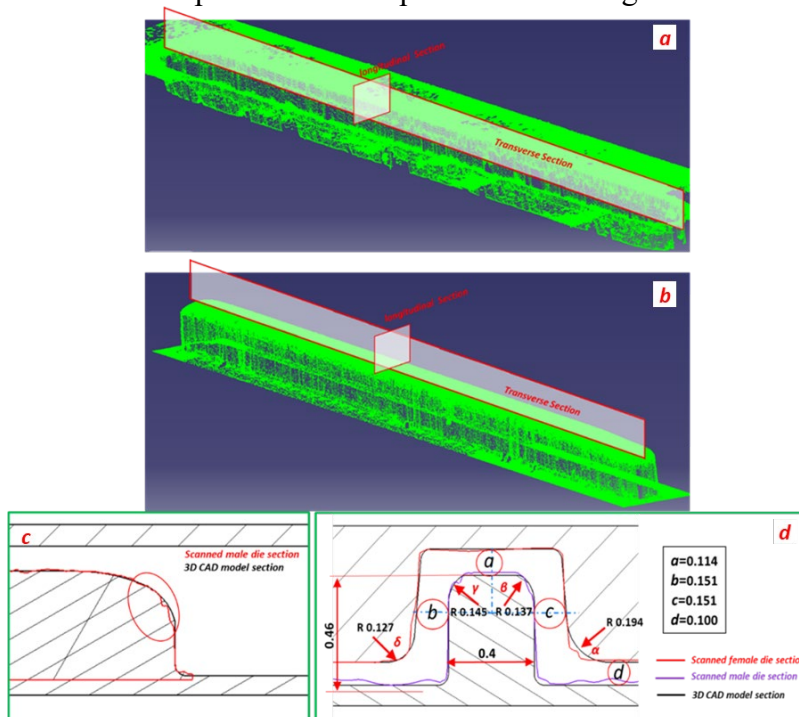

Fig. 6. a) Point cloud of female die. b) Point cloud of male die. c) Male die cross-section in longitudinal diection. d) Top and bottom die cross sections in transverse direction.

Finite Element Simulation

The commercial software package Abaqus explicit was used. Only one half of one channel was modelled in the 3D FE model. The model set up is shown in Fig. 7-a. In order to apply the force on the sheet, a displacement boundary condition is applied to the punch while the die is constrained in all directions. A symmetry boundary conditions was applied to the sheet on the symmetry axis as illustrated in Fig. 7-b (right end of the sheet). The left end was fixed to simulate the clamping of the sheet. According to the distance of the channels in transverse direction, the individual channel patterns do not influence each other during the forming process and therefore the two sides of the channel can be assumed to be fixed.

In this research, a 2D simulation was also considered to investigate the effect of different elements. Fig. 7-c demonstrates the 2D FE model. All the dimensions of FE models were considered based on the experimental set up.
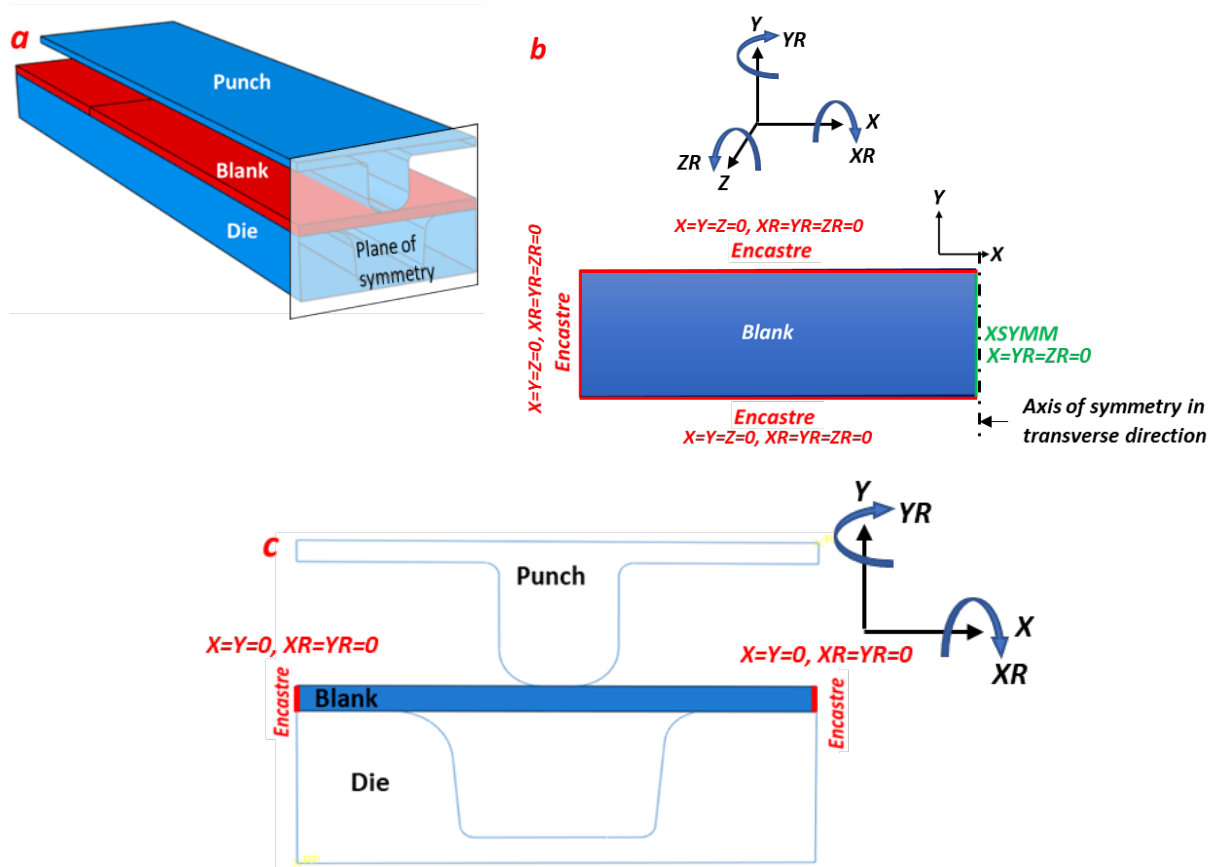

Fig. 7. a) 3D FE model for punch, die and blank. b) The boundary conditions of the blank in 3D FE model c) 2D FE model with blank boundary conditions.

The 3D geometry of the scanned punch and die surfaces profiles were converted to CAD and imported to the Abaqus explicit. The blank was modelled as a deformable part and was meshed with 3D stress, eight-node solid, reduced integration elements (C3D8R) with 10 elements through the material thickness. A mesh sensitivity study was performed to reach convergence. This gave an optimum mesh size of 0.01 mm (Fig. 8-a). For the 3D simulation with shell elements, a 4-node doubly curved thin shell (S4R) with 5 thickness integration points, reduced integration and hourglass control was used (Fig. 8-b).
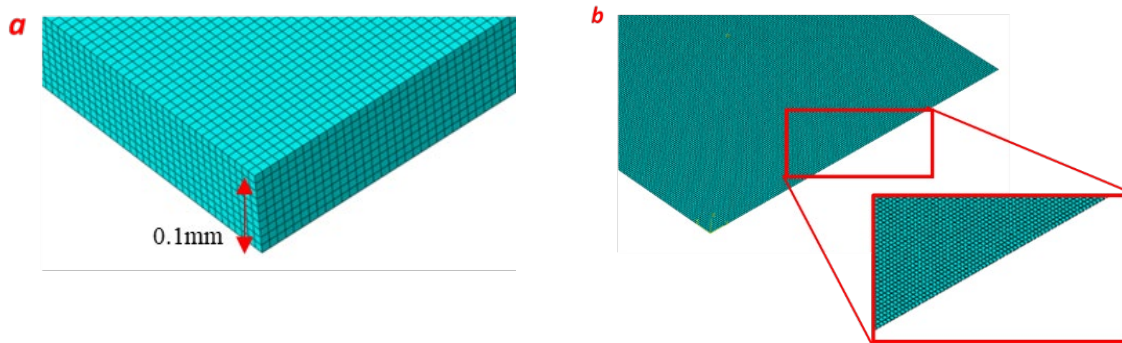
Fig. 8. FE model of the blank. a) Solid element (C3DR8) b) Shell element (S4R).

The die sets were meshed as discrete rigid bodies with four nodes of 3D bilinear rigid quadrilateral element (R3D4). The mesh size of the tools was considered in a way to discretise the geometry of the parts completely and with the desired accuracy. A refined mesh size of 0.01 mm was used in the critical contact locations of the die and the punch radius as shown in Fig. 9.

The 2D simulation was performed according to the geometry of Fig. 6, and the blank meshed with plane-strain, reduced integration CPE4R elements. The mesh size for 2D simulation was chosen the same as in previous research [16]. The Punch and die were meshed with 2-node 2-D linear discrete rigid element (R2D2). A surface-to-surface condition was implemented to define interaction between die setup and sheet.
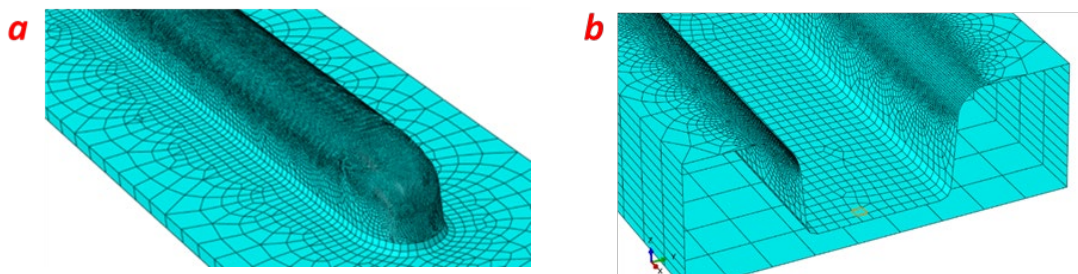

Fig. 9. FE model of the (a) punch and (b) die.

The friction coefficient between the tooling and sheet was assumed to be 0.4 in all simulations (2D and 3D) [16]. The mechanical properties of the sheets were applied in the simulation based on the material parameters given in Table 1 assuming isotropic material behaviour.

The explicit solution method used mass scaling to reduce the simulation time. The value of the mass scale coefficient (10^9) was determined in such a way that the ratio of kinetic energy to internal energy during the process was less than 1% to maintain the quasi-static nature of the problem.

Results and Discussion

The experimental thinning curves of the titanium blank are compared in the straight channel cross-section 4 mm away from the end cavities and at a punch stroke of 0.32 mm, which is when the pin hole originated. As shown in Fig. 10, the maximum thinning occurs in the die radius area. It should be noted that this is the smallest radius of the tool. Therefore, the critical forming regions are identified near the bending area of the die (δ region). The FE model represents the experimental thinning results but there is some error. This might be due to the presence of sharp points in the physical male and female tooling profile (Fig. 6-d) that were not considered in the FE model. This leads to severe deformation and, as a result, severe thinning in this area. In the FE model these

points are simplified as perfect arcs which could be why the FE model underpredicts deformation severity in this region.

There is only a minor difference in thinning prediction between the 2D and the 3D model. This may be due to material deformation being mostly plane strain tension in the investigated cross-section which is located in the straight channel and not in the end cavity. This allows for the simplification to 2D plane strain forming.
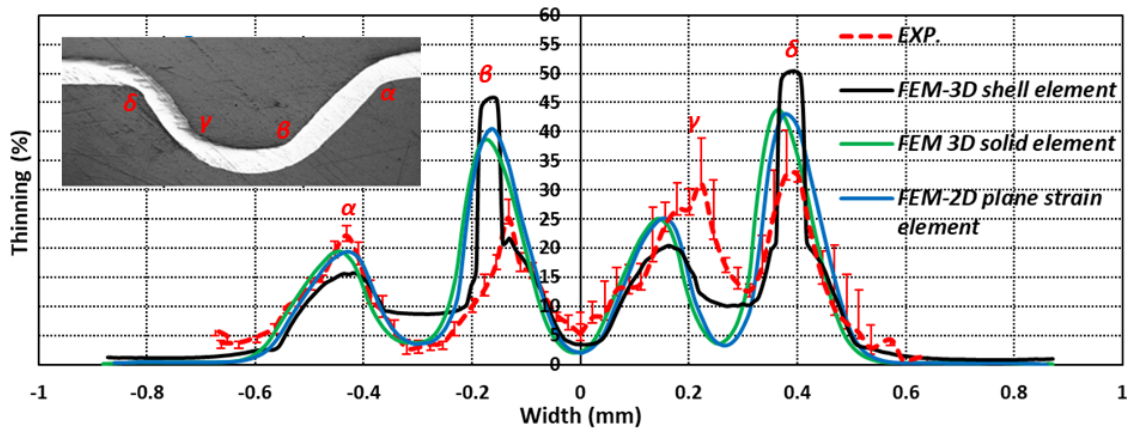

Fig. 10. Thinning prediction compared with the experimental (EXP.) results for titanium sheet.

The shell element is not able to accurately predict the distribution and level of material thinning (Fig. 10). In fact, when the punch displacement reaches to 0.26 mm, the shell element becomes extremely thin at the end of the cavity in the die area (δ region), and then thinning continues along the channel in longitudinal direction.

The thinning curves numerically predicted with the solid 3D element model for the straight channel region and the end cavity, sections 1 and 2, are shown in Fig. 11-a. There is a clear difference in the thinning behaviour between the two cross-sections (Fig. 11-b).
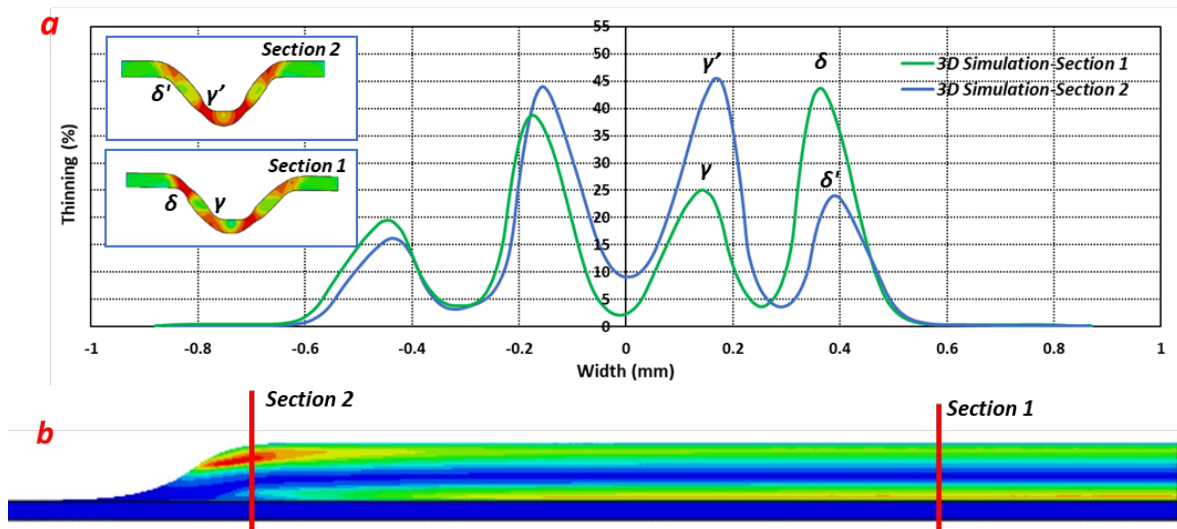

Fig. 11. a) Comparison of material thinning in sections 1 and 2. b) The location of section 1 and 2 in the simulation model.

The maximum thinning is transferred from the die radius in section 1 (region δ) to the punch radius area in section 2 (region γ'). The strain path of a node in the different radius areas was measured for both cross-sections during the process, and the result is shown in Fig. 12.

At the straight region, the strain path of the micro-channel corner regions that contact with the male and female tool radius are plane strain deformation (γ and δ Fig.12-b). The sheet at the cavity regions shows different strain path. The corner that was formed by the male tool radius region has a strain path starting with the biaxial stretching initially, but deviating to plane strain as the channel formed deeper (γ' in Fig.12-b). The female tool gives the bottom sheet corner negative minor strain (along the longitudinal of the channel direction), but the deformation mode shifts to plane strain towards the end of forming (δ' in Fig.12-b). In the cavity end area (section 2), the thinning is higher compared to the straight channel section and therefore closer to material failure. This, however, does not correlate well with the experimental pinhole location, which was in the straight channel section (Fig. 4b).
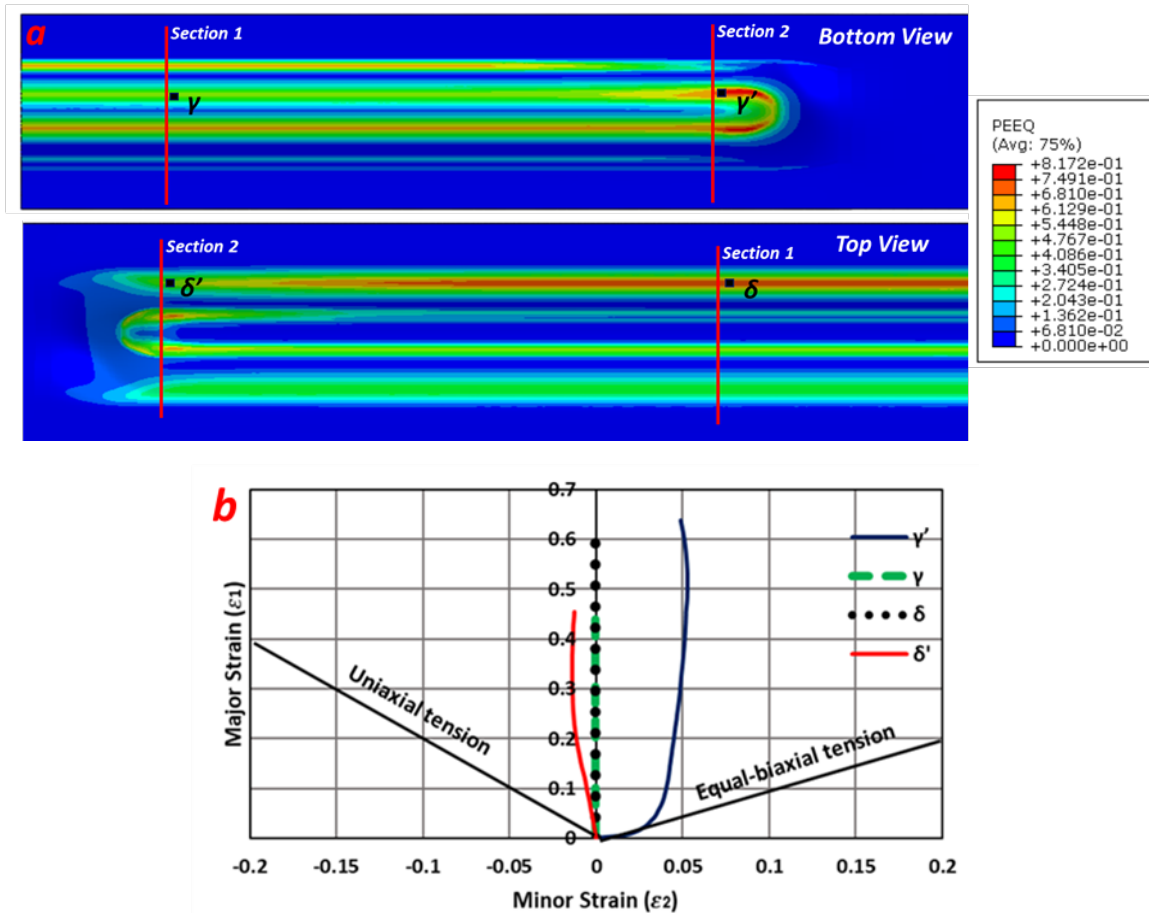

Fig. 12. a) The location of the considered nodes in the different sections, showing contours of equivalen plastic strain (PEEQ) on the bottom and top surfaces of the blank. b) The strain path of the bending area elements at both sections during the process.

Summary

- Titanium foil was micro-stamped, and the 3D FE model predictions did not match the experimental data in some of the channel regions. More research is required to accurately model the material behaviour and fracture limits of titanium foil in micro stamping.
- The analysis of solid and shell elements in the 3D model suggests that the shell elements cannot accurately represent material thinning.

- The stress state at the end cavity of the channels is different from that in the straight channel region. The assumption of 2D conditions for micro-channel deformation is therefore only valid in the straight section but does not represent the higher material deformation in the cavity that was observed in this study.
- As future work, implementing a comprehensive model that includes microstructural properties, and anisotropic properties, and performing accurate fracture criteria will be considered for the micro-stamping of the titanium foil.

References

[1] A. Hermann, T. Chaudhuri, P. Spagnol, Bipolar plates for PEM fuel cells: A review, Int. J. Hydrogen Ener. 30 (2005) 1297-1302. https://doi.org/10.1016/j.ijhydene.2005.04.016

[2] L. Carrette, K. Friedrich, U. Stimming, Fuel cells-fundamentals and applications, Fuel cells 1 (2001).

[3] J.-C. Hung, T.-C. Yang, K.-c. Li, Studies on the fabrication of metallic bipolar plates-Using micro electrical discharge machining milling, J. Power Source. 196 (2011) 2070-2074. https://doi.org/10.1016/j.jpowsour.2010.10.001

[4] L. Soler, J. Macanás, M. Munoz, J. Casado, Aluminum and aluminum alloys as sources of hydrogen for fuel cell applications, J. Power Source. 169 (2007) 144-149. https://doi.org/10.1016/j.jpowsour.2007.01.080

[5] N. Abdullah, S. Kamarudin, Titanium dioxide in fuel cell technology: An overview, J. Power Source. 278 (2015) 109-118. https://doi.org/10.1016/j.jpowsour.2014.12.014

[6] M. Weiss, P. Zhang, M.P. Pereira, B.F. Rolfe, D.E. Wilkosz, P.D. Hodgson, Understanding size effects and forming limits in the micro-stamping of industrial stainless steel foils, Metals 11 (2020) 38. https://doi.org/10.3390/met11010038

[7] R. Backes, A.M. Herring, J. Berger, J. Turner, H. Wang, Evaluation of stamping methods for stainless steel bipolar plates using finite element analysis, ECS Meeting Abstracts, IOP Publishing, 2008, p. 70. https://doi.org/10.1149/MA2008-02/1/70

[8] M. Elyasi, H.T. Ghadikolaee, M. Hosseinzadeh, Investigation of dimensional accuracy in forming of metallic bipolar plates with serpentine flow field, Int. J. Adv. Manuf. Technol. 96 (2018) 1045-1060. https://doi.org/10.1007/s00170-018-1650-5

[9] L. Peng, X. Lai, P. Hu, J. Ni, Flow channel shape optimum design for hydroformed metal bipolar plate in PEM fuel cell, J. Power Source. 178 (2008) 223-230. https://doi.org/10.1016/j.jpowsour.2007.12.037

[10] Y. Liu, L. Hua, Fabrication of metallic bipolar plate for proton exchange membrane fuel cells by rubber pad forming, J. Power Source. 195 (2010) 3529-3535. https://doi.org/10.1016/j.jpowsour.2009.12.046

[11] R. Kolahdooz, S. Asghari, S. Rashid-Nadimi, A. Amirfazli, Integration of finite element analysis and design of experiment for the investigation of critical factors in rubber pad forming of metallic bipolar plates for PEM fuel cells, Int. J. Hydro. Ener. 42 (2017) 575-589. https://doi.org/10.1016/j.ijhydene.2016.11.020

[12] M. Balali Osia, S. Jamal Hosseinipour, M. Bakhshi-Jooybari, A. Gorgi, Forming metallic micro-feature bipolar plates for fuel cell using combined hydroforming and stamping processes, Iranian (Iranica) J. Ener. Environm. 4 (2013). 10.5829/idosi.ijee.2013.04.02.03

[13] H.J. Bong, J. Lee, J.-H. Kim, F. Barlat, M.-G. Lee, Two-stage forming approach for manufacturing ferritic stainless steel bipolar plates in PEM fuel cell: Experiments and numerical simulations, Int. J Hydro. Ener. 42 (2017) 6965-6977. https://doi.org/10.1016/j.ijhydene.2016.12.094

[14] K. Karacan, S. Celik, S. Toros, M. Alkan, U. Aydin, Investigation of formability of metallic bipolar plates via stamping for light-weight PEM fuel cells, Int. J. Hydro. Ener. 45 (2020) 35149-35161. https://doi.org/10.1016/j.ijhydene.2020.01.251

[15] V. Modanloo, H. Talebi-Ghadikolaee, V. Alimirzaloo, M. Elyasi, Fracture prediction in the stamping of titanium bipolar plate for PEM fuel cells, Int. J. Hydro. Ener. 46 (2021) 5729-5739. https://doi.org/10.1016/j.ijhydene.2020.11.088

[16] P. Zhang, M.P. Pereira, B.F. Rolfe, D.E. Wilkosz, P. Hodgson, M. Weiss, Investigation of material failure in micro-stamping of metallic bipolar plates, J. Manuf. Process. 73 (2022) 54-66. https://doi.org/10.1016/j.jmapro.2021.10.044

[17] ASTM International Standard, E8M-04: Standard test methods for tension testing of metallic materials, testing of metallic materials, 2004.

[18] T. Furushima, H. Tsunezaki, K.-i. Manabe, S. Alexsandrov, Ductile fracture and free surface roughening behaviors of pure copper foils for micro/meso-scale forming, International J. Mach. Tool. Manuf. 76 (2014) 34-48. https://doi.org/10.1016/j.ijmachtools.2013.10.001

[19] B. Abeyrathna, P. Zhang, M.P. Pereira, D. Wilkosz, M. Weiss, Micro-roll forming of stainless steel bipolar plates for fuel cells, Int. J. Hydro. Ener. 44 (2019) 3861-3875. https://doi.org/10.1016/j.ijhydene.2018.12.013

[20] Information on https://www.digimizer.com/download/